

## RESEARCH ARTICLE

10.1002/2013JE004549

## Special Section:

Results from the first 360 Sols of the Mars Science Laboratory Mission: Bradbury Landing through Yellowknife Bay

## Key Points:

- Model simulation agrees with RAD measurements on Mars surface
- Dose rate varies with heliospheric condition and atmospheric pressure
- Neutron flux on Mars to be considered for radiobiology and risk assessments

## Correspondence to:

M.-H. Y. Kim,  
myung-hee.y.kim@nasa.gov

## Citation:

Kim, M.-H. Y., et al. (2014), Comparison of Martian surface ionizing radiation measurements from MSL-RAD with Badhwar-O'Neill 2011/HZETRN model calculations, *J. Geophys. Res. Planets*, 119, 1311–1321, doi:10.1002/2013JE004549.

Received 1 OCT 2013

Accepted 12 MAY 2014

Accepted article online 15 MAY 2014

Published online 17 JUN 2014

# Comparison of Martian surface ionizing radiation measurements from MSL-RAD with Badhwar-O'Neill 2011/HZETRN model calculations

Myung-Hee Y. Kim<sup>1</sup>, Francis A. Cucinotta<sup>2,3</sup>, Hatem N. Nounu<sup>1</sup>, Cary Zeitlin<sup>4</sup>, Donald M. Hassler<sup>5</sup>, Scot C. R. Rafkin<sup>5</sup>, Robert F. Wimmer-Schweingruber<sup>6</sup>, Bent Ehresmann<sup>5</sup>, David E. Brinza<sup>7</sup>, Stephan Böttcher<sup>6</sup>, Eckart Böhm<sup>6</sup>, Soenke Burmeister<sup>6</sup>, Jingnan Guo<sup>6</sup>, Jan Köhler<sup>6</sup>, Cesar Martin<sup>6</sup>, Guenther Reitz<sup>8</sup>, Arik Posner<sup>9</sup>, Javier Gómez-Elvira<sup>10</sup>, Ari-Matti Harri<sup>11</sup>, and the MSL Science Team

<sup>1</sup>Wyle Science, Technology and Engineering, Houston, Texas, USA, <sup>2</sup>NASA Johnson Space Center, Houston, Texas, USA, <sup>3</sup>University of Nevada Las Vegas, Las Vegas, Nevada, USA, <sup>4</sup>Southwest Research Institute, Durham, New Hampshire, USA, <sup>5</sup>Southwest Research Institute, Boulder, Colorado, USA, <sup>6</sup>Christian Albrechts University, Kiel, Germany, <sup>7</sup>Jet Propulsion Laboratory, California Institute of Technology, Pasadena, California, USA, <sup>8</sup>German Aerospace Center (DLR), Cologne, Germany, <sup>9</sup>NASA Headquarters, Washington, DC, USA, <sup>10</sup>Centro de Astrobiología (INTA-CSIC), Madrid, Spain, <sup>11</sup>Finnish Meteorological Institute, Helsinki, Finland

**Abstract** Dose rate measurements from Mars Science Laboratory-radiation assessment detector (MSL-RAD) for 300 sols on Mars are compared to simulation results using the Badhwar-O'Neill 2011 galactic cosmic ray (GCR) environment model and the high-charge and energy transport (HZETRN) code. For the nuclear interactions of primary GCR through Mars atmosphere and Curiosity rover, the quantum multiple scattering theory of nuclear fragmentation is used. Daily atmospheric pressure is measured at Gale Crater by the MSL Rover Environmental Monitoring Station. Particles impinging on top of the Martian atmosphere reach RAD after traversing varying depths of atmosphere that depend on the slant angles, and the model accounts for shielding of the RAD "E" detector (used for dosimetry) by the rest of the instrument. Simulation of average dose rate is in good agreement with RAD measurements for the first 200 sols and reproduces the observed variation of surface dose rate with changing heliospheric conditions and atmospheric pressure. Model results agree less well between sols 200 and 300 due to subtleties in the changing heliospheric conditions. It also suggests that the average contributions of albedo particles (charge number  $Z < 3$ ) from Martian regolith comprise about 10% and 42% of the average daily point dose and dose equivalent, respectively. Neutron contributions to tissue-averaged effective doses will be reduced compared to point dose equivalent estimates because a large portion of the neutron point dose is due to low-energy neutrons with energies  $< 1$  MeV, which do not penetrate efficiently to deep-seated tissues. However the exposures from neutrons to humans on Mars should become an important consideration in radiobiology research and risk assessment.

## 1. Introduction

The large health risks from space radiation are a limitation to the number of days astronauts could be exposed to galactic cosmic rays (GCR) for interplanetary missions [Cucinotta et al., 2013a, 2013b]. Total mortality and morbidity risks for a 940 d Mars Reference Design mission near solar minimum with large amounts of radiation shielding are estimated to exceed 5% and 10%, respectively, and with upper 95% confidence intervals more than twice these values are estimated [Cucinotta et al., 2013b]. Because of the types of radiation in space, the uncertainties in risk estimates are a major consideration for radiation protection of astronauts. The uncertainty in radiation quality effects related to cancer and other health risks is the largest uncertainty in risk estimates. Other uncertainties include the understanding of dose-rate effects, human epidemiology data, possible influence of microgravity on radiation effects, the radiation environment, and transport models. Previous comparisons of transport models to dosimetry measurements show agreement to within  $\pm 15\%$  for dose and dose equivalent on the International Space Station [Cucinotta et al., 2008] or in transit to Mars [Zeitlin et al., 2013]. However, there are many models being used in the community (Badhwar-O'Neill 2010 [O'Neill, 2010], CREME96 [Tylka et al., 1997], MCNPX [McKinney et al., 2006], FLUKA [Ballarini et al., 2007], etc.), and it is beyond the scope of this work to provide a comparison of models with each other.

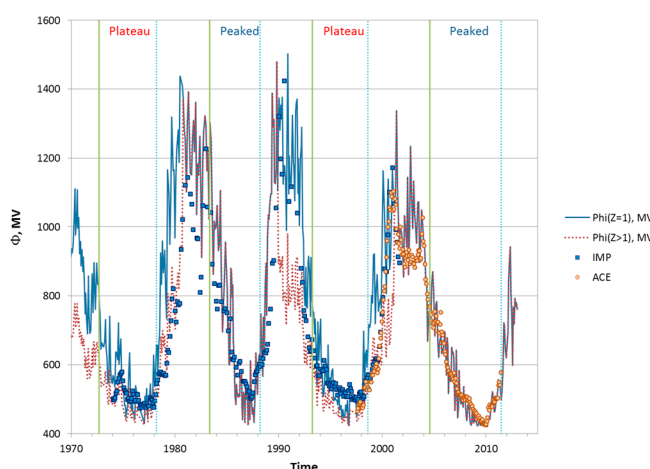


**Figure 1.** Solar modulation parameter ( $\Phi$ ) as derived from international sunspot number and from actual spacecraft instruments—Interplanetary Monitoring Platform (IMP) and Advanced Composition Explorer (ACE).

particle radiation environment [Hassler *et al.*, 2012, 2014] on the surface of Mars with roughly 30 min cadence. The RAD instrument measures both charged particle and neutral particle radiation with data products including total dose rate and particle spectra for both charged and neutral particles from roughly 10 to >100 MeV/u. Dose equivalent rates are also determined.

The purpose of this paper is to describe the comparison of the measured total dose rates of Martian surface ionization radiation for ~300 sols, with NASA's theoretical models embodied in the NASA Space Cancer Risk (NSCR-2012) model [Cucinotta *et al.*, 2013a]. The NSCR-2012 model uses the high-charge and energy (HZETRN) transport code [Wilson *et al.*, 1994] with the quantum multiple scattering theory of nuclear fragmentation (QMSFRG) cross sections [Cucinotta *et al.*, 2007] and the Badhwar-O'Neill GCR environment model [O'Neill, 2010; O'Neill and Foster, 2013].

The interplanetary plasma and radiation fields are affected by the degree of disturbance in the solar surface, and sunspot number is well correlated with many observable quantities to indicate the temporal variation of solar modulation of GCR [Kim *et al.*, 2006]. The solar modulation parameter has been derived directly from the sunspot number, with propagation delay taken into account, to determine the modulated GCR flux [O'Neill and Foster, 2013]. The GCR particles traverse the Martian atmosphere and reach the RAD instrument on the surface. Modifications to particle spectra arise from atomic interactions of charged

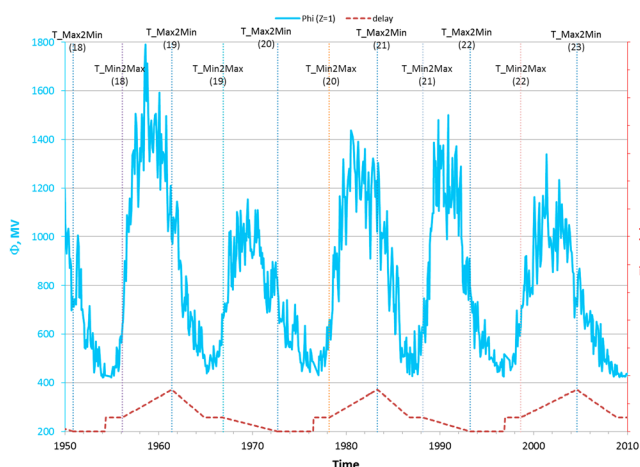


**Figure 2.** Time delay in years (brown dotted line) and the impact on the heliosphere regarding modulation of protons (light blue solid line).

Therefore, we focus our discussion here with comparison of the Mars Science Laboratory-radiation assessment detector (MSL-RAD) data to model results from Badhwar-O'Neill 2011 and high-charge and energy transport (HZETRN) models. Clearly, understanding the surface environment on Mars and how well radiation models predict this environment is an important consideration, and no comparisons were possible prior to the successful landing of Curiosity on Mars.

Since Curiosity's landing, the RAD has been measuring the energetic

particles with orbital electrons and from nuclear interactions which lead to projectile and target fragmentation. The nuclear interactions produce secondary particles such as neutrons, protons, mesons, and nuclear recoils. To determine particle transmission into RAD, calculations must consider the time-varying column depth of the atmosphere above RAD. This can be determined using the atmospheric pressure measurements of the MSL Rover Environmental Monitoring Station (REMS) [Gómez-Elvira *et al.*, 2012]. The RAD instrument's self-shielding must also be taken into account.

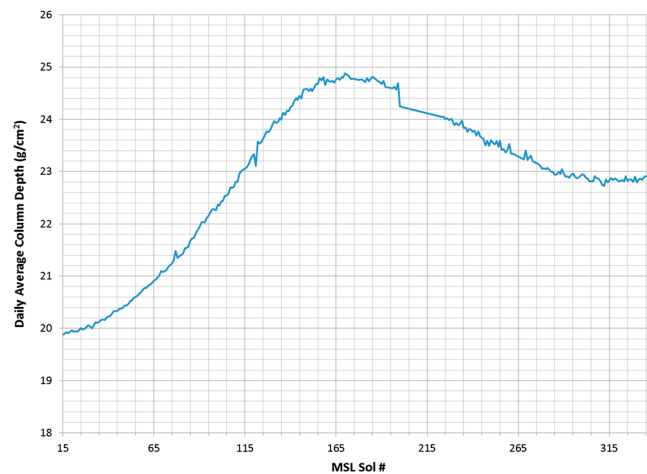


**Figure 3.** Daily average column depth measurements by the Mars Science Laboratory (MSL) Rover Environmental Monitoring Station (REMS) [Gomez-Elvira et al., 2012].

As the primary and secondary particle radiation reaches the surface, secondary neutrons are generated from the interaction of incident radiation within the Martian regolith with contributions from particles backscattered that are upward directed from the surface or in the atmosphere. The higher energy downward neutrons produced in the atmosphere and albedo neutrons and light ions contribute significantly to the complex radiation environment on the Martian surface. In this paper the forward and backscattered particles' contribution to the average daily dose and dose equivalent are evaluated over the time period corresponding to Curiosity's first 300 sols on Mars.

Validation and verification (V&V) of computational models are needed to ensure that safety factors are met for future human exploration, and to support possible developments to mitigate risks. Fortunately, radiation transport codes have been validated by extensive comparisons to measurements, and they have been combined with detailed descriptions of the space environment to enable accurate simulations behind spacecraft shielding or on planetary surfaces [Cucinotta et al., 2011; Kim et al., 2012]. Inter-comparisons of some radiation transport codes using matched configurations and environments have showed very good agreement [Heinbockel et al., 2011a, 2011b]. More importantly, transport code calculations continue to be compared to spaceflight measurements. Providing a baseline to V&V for the Badhwar-O'Neill 2011 and HZETRN model is a goal of this paper.

## 2. Galactic Cosmic Radiation Transport Through Matter

The high-charge and energy (HZETRN) transport code [Wilson et al., 1994] solves for the spectrum of nuclear fragments from projectile and target nuclei in the continuous slowing down and straight-ahead approximations or more recently using a bi-directional transport model to represent forward and backward propagations of neutrons and light particles [Wilson et al., 2004; Slaba et al., 2010]. For the nuclear interactions of the primary galactic cosmic radiation (GCR) with the matter, the quantum multiple scattering theory of nuclear fragmentation (QMSFRG) model describes the production of light nuclei through the distinct mechanisms of nuclear abrasion and ablation, coalescence, and cluster knockout [Cucinotta et al., 1997, 2007]. The QMSFRG model is shown to be in excellent agreement with available experimental data for nuclear

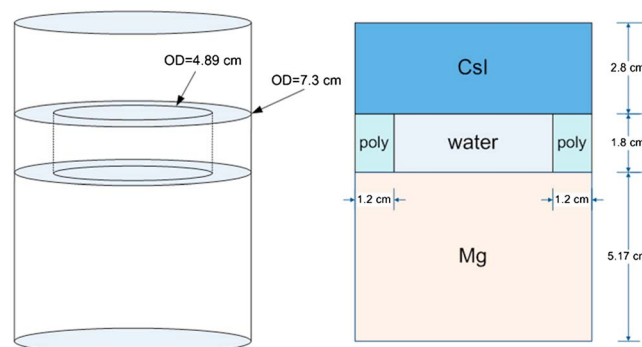


**Figure 4.** Schematic diagram and dimension of the radiation assessment detector (RAD) instrument for ray tracing.

fragmentation cross sections [Cucinotta et al., 2007]. We use the HZETRN code and the QMSFRG database to evaluate the kinetic energy ( $E$ ), mass number ( $A$ ), and charge number ( $Z$ )-dependent fluence distribution,  $F(E, A, Z)$ , after passing through matter and related dosimetric quantities.

Badhwar and O'Neill [1992] developed a self-consistent solution to the Fokker-Plank equation for particle transport in the heliosphere that has been fit to available GCR

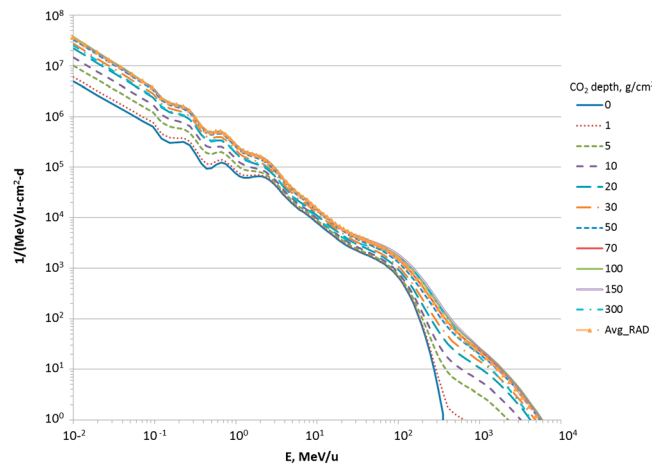


**Figure 5.** Predictions of transport model of average daily neutron spectra over 300 sols for fixed atmospheric depths and neutron spectra at the RAD detector.

model using data from the NASA Advanced Composition Explorer (ACE) for particles with charge number  $Z > 2$ . The most recent model of BO'11 [O'Neill and Foster, 2013] utilizes a large number of GCR measurements from 1955 to 2012, spanning solar cycle 19 to 24 including the recent solar minimum, which is by far the deepest minimum since space-based measurements began [Mewaldt et al., 2010]. The model calculates GCR flux by determining the solar modulation parameter,  $\Phi(t)$ , from the international sunspot number and a time delay function.

data. This model accurately accounts for solar modulation of each element (from hydrogen to nickel) by propagating the local interstellar spectrum (LIS) of each element through the heliosphere by solving the Fokker-Planck diffusion, convection, and energy loss boundary value problem. A single value of the deceleration parameter,  $\Phi(t)$ , describes the level of solar cycle modulation and determines the GCR energy spectra for all of the elements (up to plutonium  $Z = 94$ ) at a given distance from the Sun.

O'Neill [2010] has re-analyzed the

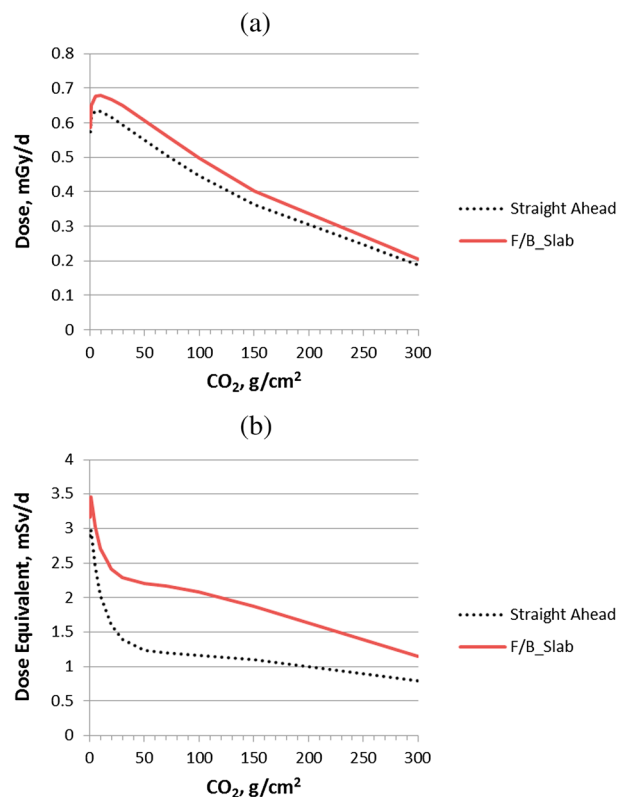


**Figure 6.** Modeled effect of albedo neutron and light particles on Mars surface as a function of Mars atmosphere from exposure to galactic cosmic ray (GCR) at 1977 solar minimum. (a) Dose and (b) dose equivalent.

### 3. Solar Modulation Parameter for GCR Flux

The intensity of the GCR flux varies over the approximately 11 year solar cycle due to changes in the interplanetary plasma that originates in the expanding solar corona [Babcock, 1961; Badhwar and O'Neill, 1992]. The intensity and energy of GCR entering the heliosphere are reduced as they are scattered by irregularities in the interplanetary magnetic field embedded in the solar wind. Parker [1965] showed that the steady-state, spherically symmetric Fokker-Planck equation accurately accounts for diffusion, convection, and adiabatic deceleration of these particles. The Fokker-Planck equation is readily solved numerically for each element to a given radius from the Sun for the propagation of the constant energy spectrum LIS at the outer edge of the heliosphere,  $\sim 100$  AU.

To account for attenuation of the LIS due to the state of the heliosphere at a specific time, Fokker-Planck equation can be expressed in terms of a single

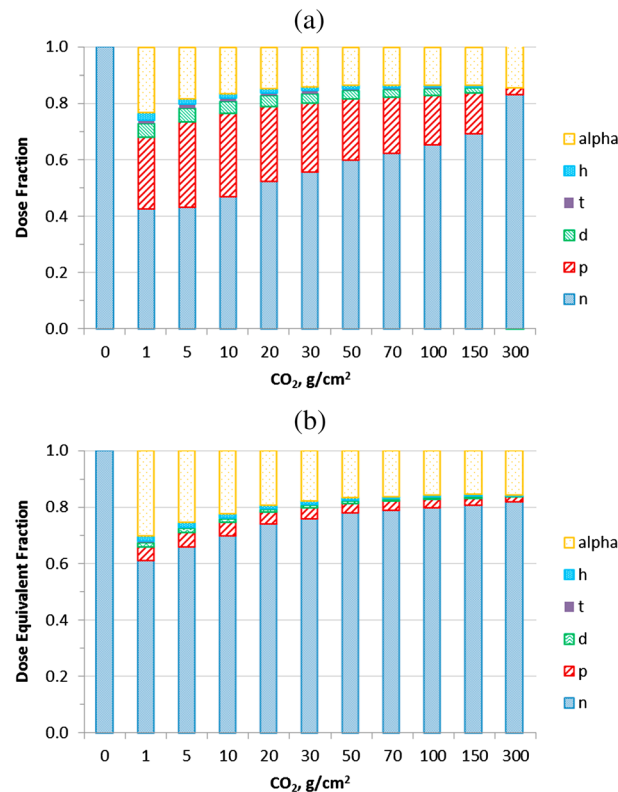


**Figure 7.** Modeled contribution of albedo neutron and light particles (proton, deuteron, triton, hellion, and  $\alpha$ ) to the backscattered dosimetric quantities on the Mars surface as a function of Mars atmosphere from exposure to GCR at 1977 solar minimum. (a) Dose and (b) dose equivalent.

time-dependent parameter, the solar modulation parameter,  $\Phi$ . Larger values of  $\Phi$  correspond to reduced GCR flux.  $\Phi$  is related to the magnetic rigidity (momentum divided by charge) required for a particle to penetrate the heliosphere [O'Neill, 2010]. Since  $\Phi$  is directly associated with solar activity, the sunspot number is used as a proxy for the temporal variation of solar modulation of GCR, and this in turn determines the modulated GCR flux for any given time. In this paper we use the most recent version of the Badhwar and O'Neill model denoted as BO'11. BO'11 uses the international sunspot number for all times with the time lag properly accounted for. The coefficient of the time delayed sunspot number for heavier particles (charge number  $Z > 1$ ) is roughly half of that for protons during the "plateau" solar minimum cycles, but the same coefficient applies to all  $Z$  during the "peaked" solar minimum cycles. The time delay is taken into account between the time of the solar activity and the time when the magnetic field disturbance

propagates into the heliosphere far enough to significantly modulate the GCR flux [Nyemik, 2000]. The resultant monthly average value of  $\Phi$  is shown in Figure 1 comparing with the measurements. Figure 2 shows the time delay used for BO'11 and the impact on the heliosphere regarding modulation of protons. The time-dependent GCR flux is evaluated on the top of Martian atmosphere using the relevant solar modulation parameters.

#### 4. Atmospheric Shielding Distribution for Martian Surface Radiation

The atmosphere of Mars attenuates the intensity of the heavy ion component of the primary GCR but increases the fluence of secondary particles (neutrons, and hydrogen and helium isotopes) because of particle production processes in nuclear interactions [Cucinotta et al., 2007]. In the prediction of surface ionizing radiation, the GCR-induced spectrum of fragments (both projectile and target nucleus fragments) produced in the atmosphere was simulated by integration over the Martian atmosphere at the RAD location. Backscattered neutrons and other light particles from the Martian regolith contribute significantly along with the GCR components [Wilson et al., 2004]. The forward and backward scattered neutrons and the backscattered light ions with mass numbers  $A \leq 4$  were simulated using a two-layer slab configuration [Slaba et al., 2010]. The dose and dose equivalent contributions from heavier target fragments with  $A > 4$  were evaluated using a local source term in water [Wilson et al., 1994]. For the bi-directional calculation at the target point on the Martian surface, a varying thickness of atmospheric slab is placed in front of the target point for each slab configuration. Mars is represented by a thick semi-infinite slab of Martian regolith which is placed behind the target point for all configurations. A depth of 1000 g/cm<sup>2</sup> below the Martian surface is considered in evaluating the albedo. The atmosphere is represented as pure carbon dioxide in the current study. Thus, the albedo analysis at the RAD detector has been made from the results of various slab configurations between atmospheric carbon dioxide thicknesses and the Martian regolith.



**Table 1.** Dose Calculation of Various Particle Types as a Function of CO<sub>2</sub> Depth From Exposure to Galactic Cosmic Ray (GCR) at 1977 Solar Minimum

Particle Type	(a) Forward Direction Only										
	0	1	5	10	20	30	50	70	100	150	300
<i>n</i>	$3.17 \times 10^{-25}$	$1.28 \times 10^{-5}$	$6.47 \times 10^{-5}$	$1.30 \times 10^{-4}$	$2.60 \times 10^{-4}$	$3.88 \times 10^{-4}$	$6.30 \times 10^{-4}$	$8.48 \times 10^{-4}$	$1.12 \times 10^{-3}$	$1.44 \times 10^{-3}$	$1.52 \times 10^{-3}$
<i>p</i>	$2.52 \times 10^{-2}$	$2.84 \times 10^{-2}$	$3.28 \times 10^{-2}$	$3.56 \times 10^{-2}$	$3.83 \times 10^{-2}$	$3.91 \times 10^{-2}$	$3.84 \times 10^{-2}$	$3.63 \times 10^{-2}$	$3.23 \times 10^{-2}$	$2.58 \times 10^{-2}$	$1.24 \times 10^{-2}$
<i>d</i>	$1.93 \times 10^{-23}$	$5.81 \times 10^{-4}$	$1.27 \times 10^{-3}$	$1.80 \times 10^{-3}$	$2.45 \times 10^{-3}$	$2.83 \times 10^{-3}$	$3.16 \times 10^{-3}$	$3.22 \times 10^{-3}$	$3.08 \times 10^{-3}$	$2.65 \times 10^{-3}$	$1.45 \times 10^{-3}$
<i>t</i>	$1.94 \times 10^{-23}$	$1.96 \times 10^{-4}$	$5.46 \times 10^{-4}$	$7.89 \times 10^{-4}$	$1.04 \times 10^{-3}$	$1.16 \times 10^{-3}$	$1.24 \times 10^{-3}$	$1.22 \times 10^{-3}$	$1.13 \times 10^{-3}$	$9.56 \times 10^{-4}$	$5.20 \times 10^{-4}$
<i>h</i>	$7.60 \times 10^{-23}$	$7.81 \times 10^{-4}$	$1.86 \times 10^{-3}$	$2.40 \times 10^{-3}$	$2.81 \times 10^{-3}$	$2.94 \times 10^{-3}$	$2.91 \times 10^{-3}$	$2.76 \times 10^{-3}$	$2.46 \times 10^{-3}$	$2.00 \times 10^{-3}$	$1.02 \times 10^{-3}$
<i>α</i>	$1.40 \times 10^{-2}$	$1.52 \times 10^{-2}$	$1.47 \times 10^{-2}$	$1.36 \times 10^{-2}$	$1.15 \times 10^{-2}$	$9.82 \times 10^{-3}$	$7.36 \times 10^{-3}$	$5.81 \times 10^{-3}$	$4.44 \times 10^{-3}$	$3.31 \times 10^{-3}$	$1.84 \times 10^{-3}$
<i>Z</i> = 3–10	$7.85 \times 10^{-3}$	$7.48 \times 10^{-3}$	$5.99 \times 10^{-3}$	$4.68 \times 10^{-3}$	$2.97 \times 10^{-3}$	$1.93 \times 10^{-3}$	$8.40 \times 10^{-4}$	$3.72 \times 10^{-4}$	$1.11 \times 10^{-4}$	$1.52 \times 10^{-5}$	$4.25 \times 10^{-8}$
<i>Z</i> = 11–20	$4.95 \times 10^{-3}$	$4.14 \times 10^{-3}$	$3.07 \times 10^{-3}$	$2.22 \times 10^{-3}$	$1.22 \times 10^{-3}$	$6.89 \times 10^{-4}$	$2.26 \times 10^{-4}$	$7.55 \times 10^{-5}$	$1.48 \times 10^{-5}$	$1.00 \times 10^{-6}$	$3.30 \times 10^{-10}$
<i>Z</i> > 20	$5.41 \times 10^{-3}$	$4.70 \times 10^{-3}$	$2.97 \times 10^{-3}$	$1.84 \times 10^{-3}$	$7.75 \times 10^{-4}$	$3.44 \times 10^{-4}$	$7.34 \times 10^{-5}$	$1.66 \times 10^{-5}$	$1.88 \times 10^{-6}$	$5.32 \times 10^{-8}$	$1.43 \times 10^{-12}$
Total	$5.74 \times 10^{-2}$	$6.15 \times 10^{-2}$	$6.33 \times 10^{-2}$	$6.31 \times 10^{-2}$	$6.14 \times 10^{-2}$	$5.92 \times 10^{-2}$	$5.48 \times 10^{-2}$	$5.06 \times 10^{-2}$	$4.47 \times 10^{-2}$	$3.62 \times 10^{-2}$	$1.88 \times 10^{-2}$
	(b) Forward and Backward Directions										
	Dose (mGy/d) at CO <sub>2</sub> Depth (g/cm <sup>2</sup> ) of										
	0	1	5	10	20	30	50	70	100	150	300
<i>n</i>	$1.22 \times 10^{-3}$	$1.36 \times 10^{-3}$	$1.83 \times 10^{-3}$	$2.32 \times 10^{-3}$	$3.05 \times 10^{-3}$	$3.53 \times 10^{-3}$	$4.10 \times 10^{-3}$	$4.38 \times 10^{-3}$	$4.50 \times 10^{-3}$	$4.31 \times 10^{-3}$	$2.86 \times 10^{-3}$
<i>p</i>	$2.52 \times 10^{-2}$	$2.92 \times 10^{-2}$	$3.40 \times 10^{-2}$	$3.70 \times 10^{-2}$	$3.97 \times 10^{-2}$	$4.05 \times 10^{-2}$	$3.97 \times 10^{-2}$	$3.74 \times 10^{-2}$	$3.33 \times 10^{-2}$	$2.64 \times 10^{-2}$	$1.25 \times 10^{-2}$
<i>d</i>	$3.86 \times 10^{-23}$	$7.30 \times 10^{-4}$	$1.47 \times 10^{-3}$	$2.01 \times 10^{-3}$	$2.65 \times 10^{-3}$	$3.02 \times 10^{-3}$	$3.33 \times 10^{-3}$	$3.37 \times 10^{-3}$	$3.20 \times 10^{-3}$	$2.72 \times 10^{-3}$	$1.45 \times 10^{-3}$
<i>t</i>	$3.88 \times 10^{-23}$	$2.39 \times 10^{-4}$	$6.03 \times 10^{-4}$	$8.47 \times 10^{-4}$	$1.10 \times 10^{-3}$	$1.22 \times 10^{-3}$	$1.28 \times 10^{-3}$	$1.26 \times 10^{-3}$	$1.16 \times 10^{-3}$	$9.72 \times 10^{-4}$	$5.16 \times 10^{-4}$
<i>h</i>	$1.52 \times 10^{-22}$	$8.70 \times 10^{-4}$	$1.95 \times 10^{-3}$	$2.48 \times 10^{-3}$	$2.90 \times 10^{-3}$	$3.02 \times 10^{-3}$	$2.98 \times 10^{-3}$	$2.82 \times 10^{-3}$	$2.51 \times 10^{-3}$	$2.03 \times 10^{-3}$	$1.02 \times 10^{-3}$
<i>α</i>	$1.40 \times 10^{-2}$	$1.59 \times 10^{-2}$	$1.55 \times 10^{-2}$	$1.44 \times 10^{-2}$	$1.23 \times 10^{-2}$	$1.06 \times 10^{-2}$	$8.15 \times 10^{-3}$	$6.57 \times 10^{-3}$	$5.13 \times 10^{-3}$	$3.87 \times 10^{-3}$	$2.09 \times 10^{-3}$
<i>Z</i> = 3–10	$7.85 \times 10^{-3}$	$7.48 \times 10^{-3}$	$5.99 \times 10^{-3}$	$4.68 \times 10^{-3}$	$2.97 \times 10^{-3}$	$1.93 \times 10^{-3}$	$8.41 \times 10^{-4}$	$3.72 \times 10^{-4}$	$1.11 \times 10^{-4}$	$1.52 \times 10^{-5}$	$4.26 \times 10^{-8}$
<i>Z</i> = 11–20	$4.95 \times 10^{-3}$	$4.14 \times 10^{-3}$	$3.07 \times 10^{-3}$	$2.22 \times 10^{-3}$	$1.22 \times 10^{-3}$	$6.90 \times 10^{-4}$	$2.26 \times 10^{-4}$	$7.55 \times 10^{-5}$	$1.48 \times 10^{-5}$	$1.00 \times 10^{-6}$	$3.31 \times 10^{-10}$
<i>Z</i> > 20	$5.41 \times 10^{-3}$	$4.70 \times 10^{-3}$	$2.97 \times 10^{-3}$	$1.84 \times 10^{-3}$	$7.75 \times 10^{-4}$	$3.45 \times 10^{-4}$	$7.34 \times 10^{-5}$	$1.66 \times 10^{-5}$	$1.88 \times 10^{-6}$	$5.32 \times 10^{-8}$	$1.43 \times 10^{-12}$
Total	$5.86 \times 10^{-2}$	$6.46 \times 10^{-2}$	$6.74 \times 10^{-2}$	$6.78 \times 10^{-2}$	$6.67 \times 10^{-2}$	$6.49 \times 10^{-2}$	$6.07 \times 10^{-2}$	$5.63 \times 10^{-2}$	$4.99 \times 10^{-2}$	$4.03 \times 10^{-2}$	$2.04 \times 10^{-2}$

The atmospheric pressure has been measured by the MSL Rover Environmental Monitoring Station (REMS) [Gómez-Elvira *et al.*, 2012]. Daily average column depths are shown in Figure 3. The Martian surface radiation environment is determined by integrating the spherically distributed atmospheric distances, where the target point is simulated and the contributions of albedo neutrons and light particles are evaluated for various heliospheric conditions in the comparisons below.

## 5. Geometry of the RAD Instrument for Ray Tracing at the Target Point

The RAD instrument is mounted just below the top deck of the Curiosity rover with the charged particle telescope pointed in the zenith direction. The field of view of the charged particle telescope is unobstructed. In the assessment of the shielding thickness encountered by rays that traverse the atmosphere and reach the RAD, only those rays which correspond to downward directions above the RAD horizon are considered. A semi-infinite slab of Martian regolith shielding negates any forward propagating particles below the planet horizon. The RAD instrument consists of a charged particle telescope of Si detectors, the scintillating plastic (referred to as the E-detector), and a CsI crystal for the detection of neutral particles. In Figure 4, the geometry of the RAD is approximated as a cylindrical instrument to quantify the detector's self-shielding. In this schematic diagram, the water-equivalent E-detector is surrounded by an anti-coincidence shield of scintillating polystyrene in the center, and the 12.6 g/cm<sup>2</sup> CsI and the 9 g/cm<sup>2</sup> electronics box (approximated as consisting purely of Mg) are placed above and below the E-detector, respectively. The shielding by other components, including three 300 micron thick Si detectors, and two very thin windows is not modeled; these pieces are negligible compared to the shielding provided by the atmosphere and other detectors.

For the assessment of the atmospheric shielding at the position of the RAD detector, a shielding distribution is derived for each fixed vertical column depth, which varies with daily pressure using Pro/Engineer CAD tool with NASA-developed "Fishbowl" tool kit package [Ponomarev *et al.*, 2007; Nounu *et al.*, 2009]. The resulting distribution of weighted distances is used for the HZETRN results in order to integrate over the variable atmospheric shielding. Homogeneously spaced rays originate from the target point, which is placed at the center of the E-detector, and travel to each part of the RAD in order to determine the directional shielding. Radiation fields at the target point are computed using a ray-by-ray transport to account for the RAD instrument shielding along each ray. The electronics box is below the horizon of the target point and is neglected in this part of the calculation. Also, the contributions of neutrons produced in the rover have not been included at this time. The differences in production cross sections and transport between regolith and the rover should be considered in future work to improve understanding of albedo components.

**Table 2.** Dose Equivalent Calculation of Various Particle Types as a Function of CO<sub>2</sub> Depth from Exposure to GCR at 1977 Solar Minimum

(a) Forward Direction Only												
Particle Type	Dose Equivalent (mSv/d) at CO <sub>2</sub> Depth (g/cm <sup>2</sup> ) of											
	0	1	5	10	20	30	50	70	100	150	300	
<i>n</i>	5.23 × 10 <sup>-24</sup>	2.55 × 10 <sup>-4</sup>	1.29 × 10 <sup>-3</sup>	2.59 × 10 <sup>-3</sup>	5.22 × 10 <sup>-3</sup>	7.81 × 10 <sup>-3</sup>	1.28 × 10 <sup>-2</sup>	1.73 × 10 <sup>-2</sup>	2.30 × 10 <sup>-2</sup>	2.96 × 10 <sup>-2</sup>	3.16 × 10 <sup>-2</sup>	
<i>p</i>	3.00 × 10 <sup>-2</sup>	3.67 × 10 <sup>-2</sup>	4.27 × 10 <sup>-2</sup>	4.64 × 10 <sup>-2</sup>	4.99 × 10 <sup>-2</sup>	5.11 × 10 <sup>-2</sup>	5.03 × 10 <sup>-2</sup>	4.78 × 10 <sup>-2</sup>	4.30 × 10 <sup>-2</sup>	3.48 × 10 <sup>-2</sup>	1.74 × 10 <sup>-2</sup>	
<i>d</i>	2.72 × 10 <sup>-23</sup>	1.71 × 10 <sup>-3</sup>	2.75 × 10 <sup>-3</sup>	3.51 × 10 <sup>-3</sup>	4.45 × 10 <sup>-3</sup>	5.00 × 10 <sup>-3</sup>	5.53 × 10 <sup>-3</sup>	5.65 × 10 <sup>-3</sup>	5.51 × 10 <sup>-3</sup>	4.91 × 10 <sup>-3</sup>	2.95 × 10 <sup>-3</sup>	
<i>t</i>	2.84 × 10 <sup>-23</sup>	5.31 × 10 <sup>-4</sup>	1.09 × 10 <sup>-3</sup>	1.46 × 10 <sup>-3</sup>	1.85 × 10 <sup>-3</sup>	2.04 × 10 <sup>-3</sup>	2.19 × 10 <sup>-3</sup>	2.20 × 10 <sup>-3</sup>	2.11 × 10 <sup>-3</sup>	1.86 × 10 <sup>-3</sup>	1.12 × 10 <sup>-3</sup>	
<i>h</i>	9.55 × 10 <sup>-23</sup>	3.88 × 10 <sup>-3</sup>	6.83 × 10 <sup>-3</sup>	8.15 × 10 <sup>-3</sup>	9.22 × 10 <sup>-3</sup>	9.64 × 10 <sup>-3</sup>	9.83 × 10 <sup>-3</sup>	9.65 × 10 <sup>-3</sup>	9.10 × 10 <sup>-3</sup>	7.95 × 10 <sup>-3</sup>	4.71 × 10 <sup>-3</sup>	
<i>α</i>	1.66 × 10 <sup>-2</sup>	3.46 × 10 <sup>-2</sup>	3.68 × 10 <sup>-2</sup>	3.70 × 10 <sup>-2</sup>	3.64 × 10 <sup>-2</sup>	3.58 × 10 <sup>-2</sup>	3.49 × 10 <sup>-2</sup>	3.43 × 10 <sup>-2</sup>	3.33 × 10 <sup>-2</sup>	3.12 × 10 <sup>-2</sup>	2.17 × 10 <sup>-2</sup>	
<i>Z</i> = 3–10	4.85 × 10 <sup>-2</sup>	4.60 × 10 <sup>-2</sup>	3.35 × 10 <sup>-2</sup>	2.42 × 10 <sup>-2</sup>	1.39 × 10 <sup>-2</sup>	8.35 × 10 <sup>-3</sup>	3.22 × 10 <sup>-3</sup>	1.29 × 10 <sup>-3</sup>	3.40 × 10 <sup>-4</sup>	3.91 × 10 <sup>-5</sup>	7.84 × 10 <sup>-8</sup>	
<i>Z</i> = 11–20	8.51 × 10 <sup>-2</sup>	6.74 × 10 <sup>-2</sup>	4.87 × 10 <sup>-2</sup>	3.45 × 10 <sup>-2</sup>	1.85 × 10 <sup>-2</sup>	1.02 × 10 <sup>-2</sup>	3.23 × 10 <sup>-3</sup>	1.04 × 10 <sup>-3</sup>	1.94 × 10 <sup>-4</sup>	1.21 × 10 <sup>-5</sup>	3.26 × 10 <sup>-9</sup>	
<i>Z</i> > 20	1.10 × 10 <sup>-1</sup>	9.71 × 10 <sup>-2</sup>	6.42 × 10 <sup>-2</sup>	4.09 × 10 <sup>-2</sup>	1.78 × 10 <sup>-2</sup>	8.12 × 10 <sup>-3</sup>	1.79 × 10 <sup>-3</sup>	4.14 × 10 <sup>-4</sup>	4.81 × 10 <sup>-5</sup>	1.40 × 10 <sup>-6</sup>	3.88 × 10 <sup>-11</sup>	
Total	2.90 × 10 <sup>-1</sup>	2.88 × 10 <sup>-1</sup>	2.38 × 10 <sup>-1</sup>	1.99 × 10 <sup>-1</sup>	1.57 × 10 <sup>-1</sup>	1.38 × 10 <sup>-1</sup>	1.24 × 10 <sup>-1</sup>	1.20 × 10 <sup>-1</sup>	1.17 × 10 <sup>-1</sup>	1.10 × 10 <sup>-1</sup>	7.95 × 10 <sup>-2</sup>	
(b) Forward and Backward Directions												
Particle Type	Dose Equivalent (mSv/d) at CO <sub>2</sub> Depth (g/cm <sup>2</sup> ) of											
	0	1	5	10	20	30	50	70	100	150	300	
<i>n</i>	2.61 × 10 <sup>-2</sup>	2.91 × 10 <sup>-2</sup>	3.91 × 10 <sup>-2</sup>	4.97 × 10 <sup>-2</sup>	6.54 × 10 <sup>-2</sup>	7.58 × 10 <sup>-2</sup>	8.80 × 10 <sup>-2</sup>	9.38 × 10 <sup>-2</sup>	9.64 × 10 <sup>-2</sup>	9.21 × 10 <sup>-2</sup>	6.11 × 10 <sup>-2</sup>	
<i>p</i>	3.00 × 10 <sup>-2</sup>	3.90 × 10 <sup>-2</sup>	4.57 × 10 <sup>-2</sup>	4.97 × 10 <sup>-2</sup>	5.33 × 10 <sup>-2</sup>	5.45 × 10 <sup>-2</sup>	5.36 × 10 <sup>-2</sup>	5.09 × 10 <sup>-2</sup>	4.56 × 10 <sup>-2</sup>	3.68 × 10 <sup>-2</sup>	1.81 × 10 <sup>-2</sup>	
<i>d</i>	5.44 × 10 <sup>-23</sup>	2.45 × 10 <sup>-3</sup>	3.58 × 10 <sup>-3</sup>	4.37 × 10 <sup>-3</sup>	5.31 × 10 <sup>-3</sup>	5.86 × 10 <sup>-3</sup>	6.33 × 10 <sup>-3</sup>	6.39 × 10 <sup>-3</sup>	6.13 × 10 <sup>-3</sup>	5.36 × 10 <sup>-3</sup>	3.06 × 10 <sup>-3</sup>	
<i>t</i>	5.69 × 10 <sup>-23</sup>	7.66 × 10 <sup>-4</sup>	1.35 × 10 <sup>-3</sup>	1.72 × 10 <sup>-3</sup>	2.11 × 10 <sup>-3</sup>	2.30 × 10 <sup>-3</sup>	2.43 × 10 <sup>-3</sup>	2.41 × 10 <sup>-3</sup>	2.28 × 10 <sup>-3</sup>	1.98 × 10 <sup>-3</sup>	1.13 × 10 <sup>-3</sup>	
<i>h</i>	1.91 × 10 <sup>-22</sup>	4.83 × 10 <sup>-3</sup>	7.79 × 10 <sup>-3</sup>	9.10 × 10 <sup>-3</sup>	1.02 × 10 <sup>-2</sup>	1.06 × 10 <sup>-2</sup>	1.07 × 10 <sup>-2</sup>	1.04 × 10 <sup>-2</sup>	9.72 × 10 <sup>-3</sup>	8.37 × 10 <sup>-3</sup>	4.75 × 10 <sup>-3</sup>	
<i>α</i>	1.66 × 10 <sup>-2</sup>	4.89 × 10 <sup>-2</sup>	5.15 × 10 <sup>-2</sup>	5.21 × 10 <sup>-2</sup>	5.22 × 10 <sup>-2</sup>	5.19 × 10 <sup>-2</sup>	5.11 × 10 <sup>-2</sup>	5.00 × 10 <sup>-2</sup>	4.79 × 10 <sup>-2</sup>	4.33 × 10 <sup>-2</sup>	2.74 × 10 <sup>-2</sup>	
<i>Z</i> = 3–10	4.85 × 10 <sup>-2</sup>	4.60 × 10 <sup>-2</sup>	3.35 × 10 <sup>-2</sup>	2.42 × 10 <sup>-2</sup>	1.39 × 10 <sup>-2</sup>	8.35 × 10 <sup>-3</sup>	3.22 × 10 <sup>-3</sup>	1.29 × 10 <sup>-3</sup>	3.40 × 10 <sup>-4</sup>	3.91 × 10 <sup>-5</sup>	7.84 × 10 <sup>-8</sup>	
<i>Z</i> = 11–20	8.51 × 10 <sup>-2</sup>	6.74 × 10 <sup>-2</sup>	4.87 × 10 <sup>-2</sup>	3.45 × 10 <sup>-2</sup>	1.85 × 10 <sup>-2</sup>	1.02 × 10 <sup>-2</sup>	3.23 × 10 <sup>-3</sup>	1.04 × 10 <sup>-3</sup>	1.94 × 10 <sup>-4</sup>	1.21 × 10 <sup>-5</sup>	3.26 × 10 <sup>-9</sup>	
<i>Z</i> > 20	1.10 × 10 <sup>-1</sup>	9.71 × 10 <sup>-2</sup>	6.42 × 10 <sup>-2</sup>	4.09 × 10 <sup>-2</sup>	1.78 × 10 <sup>-2</sup>	8.12 × 10 <sup>-3</sup>	1.79 × 10 <sup>-3</sup>	4.14 × 10 <sup>-4</sup>	4.81 × 10 <sup>-5</sup>	1.40 × 10 <sup>-6</sup>	3.88 × 10 <sup>-11</sup>	
Total	3.16 × 10 <sup>-1</sup>	3.36 × 10 <sup>-1</sup>	2.95 × 10 <sup>-1</sup>	2.66 × 10 <sup>-1</sup>	2.39 × 10 <sup>-1</sup>	2.28 × 10 <sup>-1</sup>	2.20 × 10 <sup>-1</sup>	2.17 × 10 <sup>-1</sup>	2.09 × 10 <sup>-1</sup>	1.88 × 10 <sup>-1</sup>	1.16 × 10 <sup>-1</sup>	

## 6. Predictions of the Transport Model

Transport code calculations were made for the case of only forward contributions and a second case which included the backward propagation. The difference between neutron spectra between these two cases thus represents the albedo neutron contribution. Figure 5 shows the daily average energy spectra of neutrons over 300 sols for fixed atmospheric depths and prediction at the RAD detector after integration over the Martian atmosphere. The effect of albedo neutrons and light ions is shown in Figures 6a and 6b. Without any atmospheric shielding, the albedo neutrons contribute 2% and 8% of total point dose and total point-dose equivalent, respectively. The contributions of backscattered neutrons and light ions to dose and dose equivalent increase to 10% and 45%, respectively, for CO<sub>2</sub> shielding depths between 50 and 150 g/cm<sup>2</sup> and then decrease beyond those depths. The separate effects of albedo neutrons and light particles to the total backscattered dose and dose equivalent are found as the fraction to the total increased quantities by albedo particles (*n*, *p*, *d*, *t*, *h*, and *α*) in Figures 7a and 7b from the calculated doses and dose equivalents of various particle types from exposure to GCR at 1977 solar minimum in Tables 1 and 2, respectively, for the forward direction only and the forward and backward directions. Here, the largest contribution is from albedo neutrons. The remaining contribution to the backscattered dose is from protons and helium ions, but contributions to dose equivalent are largely from backscattered helium ions. Dose contributions from gamma rays produced by albedo neutrons have not been estimated. Their contribution to dose equivalent is likely to be small because of their low quality factors, but such gamma rays increase absorbed doses by a few percent and should be investigated.

In considering predictions from transport models of neutron contribution to doses at the RAD detector, it needs to be noted that for radiation protection considerations the addition of tissue shielding will greatly reduce low-energy (<1 MeV) neutron contributions to tissue averaged doses or effective dose equivalents [ICRP, 2013]. The calculations made here for point doses, which are defined as without tissue shielding, will overestimate the percent contribution of neutrons to tissue averaged doses or effective dose equivalent, which are important quantities for human risk assessment.

As heliospheric condition changes from solar maximum to solar minimum, the relative contribution of albedo particles to the total dose and the dose equivalent increases regardless of atmospheric depth. This is because the GCR energy spectra at solar minimum are populated at low energies compared to solar maximum, and a larger share of primary GCRs fail to penetrate the atmosphere. The high-energy, highly penetrating particles that generate albedo particles are largely unaffected by the changing heliospheric conditions; hence, their contribution remains nearly constant. Table 3 shows predictions of the albedo neutron contributions to point doses and dose equivalents for increasing atmospheric depths. The contributions peak at the

**Table 3.** Contribution of Albedo Particles

CO <sub>2</sub> , g/cm <sup>2</sup>	Heliospheric Condition				
	Large Solar Maximum	Average Solar Maximum	Median Solar Activity	Average Solar Minimum	Deep Solar Minimum
<i>Contribution to the Total Dose</i>					
0	2.1%	2.1%	2.9%	3.4%	2.3%
1	4.8%	4.9%	6.7%	7.6%	5.4%
5	6.0%	6.1%	8.0%	9.0%	6.6%
10	6.9%	6.9%	8.8%	9.9%	7.5%
20	8.0%	8.0%	9.9%	11.0%	8.6%
30	8.7%	8.7%	10.6%	11.7%	9.4%
50	9.6%	9.6%	11.3%	12.2%	10.2%
70	10.1%	10.1%	11.6%	12.4%	10.6%
100	10.4%	10.4%	11.6%	12.4%	10.9%
150	10.3%	10.3%	11.2%	11.8%	10.7%
300	7.9%	7.9%	8.7%	9.2%	8.3%
<i>Contribution to the Total Dose Equivalent</i>					
0	8.2%	8.2%	8.9%	10.4%	11.5%
1	13.7%	13.7%	14.6%	16.6%	18.2%
5	19.0%	19.0%	19.9%	21.6%	23.1%
10	24.9%	24.9%	25.8%	27.5%	28.9%
20	33.7%	33.7%	34.7%	36.5%	38.0%
30	39.1%	39.1%	40.2%	42.1%	43.6%
50	43.7%	43.7%	44.8%	46.7%	48.2%
70	44.7%	44.8%	45.8%	47.4%	48.9%
100	44.1%	44.1%	45.0%	46.4%	47.6%
150	41.2%	41.2%	42.0%	43.2%	44.3%
300	31.1%	31.2%	32.0%	33.1%	34.2%

atmospheric depths between 50 and 150 g/cm<sup>2</sup>, and are nearly constant in that range. Above 150 g/cm<sup>2</sup>, the albedo contributions decline due to the decreasing rate of production of new particles beyond this depth. Although there is presently no place on Mars where the vertical atmospheric shielding is as great as 50 g/cm<sup>2</sup>, the contributions at greater depths are of interest when considering particles propagating or produced along the horizon and for earlier epochs in which Mars is believed to have had a much more massive atmosphere.

## 7. Dose and Dose Equivalent on Martian Surface

Figure 8 shows the comparisons of RAD measurements of dose rate to the simulation of NASA's HZETRN model with the QMSFRG database [Cucinotta *et al.*, 2013a] and the additional dose contributions from albedo particles [Slaba *et al.*, 2010] with a systematic correction for pion production included, which is based on the recent comparisons of HZETRN results to measurements [Aghara *et al.*, 2009; Sato *et al.*, 2011; Slaba *et al.*,

2013]. The RAD data and model calculations for the average daily dose rate are in good agreement. For these calculations, a running daily solar modulation parameter is used, which is evaluated using the monthly average smoothed sunspot number averaged over the month prior to the dose prediction, and REMS data [Gómez-Elvira *et al.*, 2012] for the average daily Martian surface pressure are used to evaluate the variable column depth of CO<sub>2</sub> for the calculation. The average quality factor,  $\langle Q \rangle$  is predicted to be about 2.3 for the downward GCR and associated secondaries. The mean

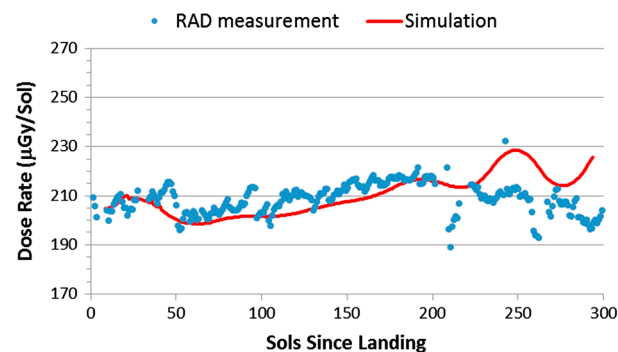


**Figure 8.** Model (red) using Badhwar-O'Neill 2011 and high-charge and energy transport (HZETRN) and RAD measurements (black) of the Martian surface radiation dose rate.



values of the albedo contribution at the RAD detector comprise 10% of the dose and 42% of the dose equivalent, and inclusion of this contribution increases the average quality factor to 3.5.

The RAD data and model calculations for the average daily dose rate are in relatively good agreement for the first 200 sols. However, model results agree less well between sols 200 and 300, which is thought to be due to subtleties in the changing heliospheric conditions which are not adequately modeled using the modulation parameter ( $\Phi$ ). On the Mars surface, during ~300 sol period near the maximum of solar cycle 24, an average total GCR dose rate at Gale Crater (−4.4 km Mars orbital laser altimeter) was found to be  $0.21 \pm 0.01$  mGy/sol from the simulation, compared to  $0.21 \pm 0.05$  mGy/sol by the RAD measurement using the E-detector [Hassler *et al.*, 2014]. The average quality factor  $\langle Q \rangle$  on the Martian surface was estimated as  $3.5 \pm 0.02$  from the simulation, compared to  $3.05 \pm 0.3$  by the RAD measurement [Hassler *et al.*, 2014]. The larger value of  $\langle Q \rangle$  predicted by the simulation is likely due to the fact that RAD E-detector is insensitive to neutrons with energies below about 5 MeV. Neutron doses obtained using RAD's plastic scintillator and CsI crystal detector will be reported in the future.

The resultant average GCR dose equivalent rate on the Mars surface is  $0.72 \pm 0.02$  mSv/sol from the simulation, compared to  $0.66 \pm 0.10$  mSv/sol from combining the tissue dose-rate measurement with  $\langle Q \rangle$  measurement by the RAD [Hassler *et al.*, 2014]. We have not modeled particles produced in the shielding provided by the rover and by those components in the geometry of the RAD instrument, which should be considerations for future investigations.

## 8. Summary and Conclusion

The absorbed dose and dose equivalent from galactic cosmic rays (GCR) have been reported after consideration of the measured linear energy transfer spectra on the surface of Mars at Gale Crater by the radiation assessment detector (RAD) instrument for ~300 sols of observations since the landing on 6 August 2012 [Hassler *et al.*, 2014]. These surface measurements provide necessary “ground truth” data to validate simulations of radiation fields on the Mars surface, to which astronauts and microelectronics will be subjected. The simulated total dose rates using Badhwar-O'Neill 2011 and HZETRN agrees on average to within  $\pm 15\%$  with the RAD measurements and reproduces the observed variation of surface dose rate with changing heliospheric conditions and atmospheric pressure [Rafkin *et al.*, 2014].

The time-dependent GCR environments are calculated by using the Badhwar-O'Neill 2011 (BO'11) GCR model during those periods sol-by-sol accounting for heliospheric condition in terms of the solar modulation. In the estimates of the surface radiation environment observed by the RAD instrument, transport calculations considered the detector self-shielding and the daily changes in the shielding provided by the Mars atmosphere. For the later, the daily atmospheric pressure measurement at Gale Crater in the southern hemisphere by the MSL Rover Environmental Monitoring Station (REMS) was used to evaluate the spherically distributed atmospheric shielding distribution. Nuclear fragmentation and energy loss processes of the primary GCR through the Martian atmosphere and the RAD instrument shielding are simulated by using the HZETRN code and a quantum multiple scattering model of nuclear fragmentation (QMSFRG). Additional contributions from albedo neutrons and light particles are analyzed by using HZETRN2010 [Slaba *et al.*, 2010] with NUCFRG3 [Adamczyk *et al.*, 2012] from the slab configuration between the Martian atmosphere and the Martian regolith as a function of heliospheric condition.

In the current simulation, any effects of the GCR dose rate due to short-term heliospheric structure variability due to solar activity and rotation are not included. The resultant time series of dose rate simulation compared to the RAD measurement show relatively good agreement, with the simulations reproducing the observed variation of surface dose rate with changing heliospheric conditions and atmospheric pressure. The comparison here of the NASA computational models with the RAD data shows relatively good agreement in terms of total dose rate measurements. However, further comparisons of charged particle spectra as well as neutron spectra will be critical for ultimately validating any radiation transport model. To date, RAD has only observed a dose rate enhancement from one moderately hard Solar Energetic Particle event on sol 242 (12–13 April 2013), and several dose rate decreases from Forbush decreases [Cane, 2000] resulting from soft event-related interplanetary coronal mass ejections on sols 50, 97, 208, and 259 [Hassler *et al.*, 2014]. Future work should consider comparisons of SPE propagation models with the RAD data sets and the comparison of the surface measurements from future hard and soft events as they occur through the remainder of this solar maximum and into the upcoming solar minimum.

The present results provide the first step in validating accurate estimates of organ dose, and the resultant biological risks can be made to evaluate radiation shielding requirements for varying space scenarios using the NASA's space radiation evaluation tool, the NSCR-2012 model [Cucinotta *et al.*, 2013a, 2013b]. The next step will be to compare measured charged particle spectra and measured neutron spectra with the NASA NSCR-2012 tool, as well as other transport models being used throughout the community. The NSCR-2012 incorporates the computational models used herein and the comparisons made possible by the RAD instrument so far improve confidence in the application of the NSCR-2012 model for mission design considerations. The estimates here of neutrons contributions to point dose equivalents of more than 40% likely over-estimate the neutron contributions to effective dose equivalents or risks because of the large contributions from neutrons with energies below 1 MeV, which do not penetrate efficiently to deep-seated tissues [ICRP, 2013]. However, the large contribution to exposures from neutrons to humans visiting Mars should become an important consideration to radiobiology research and risk assessments.

### Acknowledgments

RAD is supported by NASA (HEOMD) under Jet Propulsion Laboratory (JPL) subcontract 1273039 to Southwest Research Institute and in Germany by the German Aerospace Center (DLR) and DLR's Space Administration grant 50QM0501 and 50QM1201 to the Christian-Albrechts-Universität Kiel. Part of this research was carried out at JPL, California Institute of Technology, under a contract with NASA. We thank Jeff Simmonds, John Grotzinger, Joy Crisp, Ashwin Vasvada, and Helen Mortensen at JPL, Gale Allen, Michael Meyer, Chris Moore, Victoria Friedensen at NASA Headquarters, and Heiner Witte at DLR in Germany for their support of RAD. The data used in this paper are archived in the NASA Planetary Data System's Planetary Plasma Interactions Node at the University of California, Los Angeles. The archival volume includes the full binary raw data files, detailed descriptions of the structures therein, and higher-level data products in human-readable form. The PPI node is hosted at the following URL: <http://ppi.pds.nasa.gov/>. We appreciate helpful discussion in BO'11 with Dr. Patrick O'Neill at the NASA Johnson Space Center and in HZETRN with Dr. Francis Badavi at the NASA Langley Research Center.

### References

- Adamczyk, A. M., R. B. Norman, S. I. Sriprisan, L. W. Townsend, J. W. Norbury, S. R. Blattnig, and T. C. Slaba (2012), NUCFRG3: Light ion improvements to the nuclear fragmentation model, *Nucl. Instrum. Methods Phys. Res., Sect. A*, 678, 21–32.
- Aghara, S. K., S. R. Blattnig, J. W. Norbury, and R. C. Singleterry (2009), Monte Carlo analysis of pion contribution to absorbed dose from galactic cosmic rays, *Nucl. Instrum. Methods Phys. Res., Sect. B*, 264, 1115–1124.
- Babcock, H. W. (1961), The topology of the Sun's magnetic field and the 22-year cycle, *Astrophys. J.*, 133(2), 572–587.
- Badhwar, G. D., and P. M. O'Neill (1992), An improved model of galactic cosmic radiation for space exploration missions, *Nucl. Tracks Radiat. Meas.*, 20, 403–410.
- Ballarini, F., et al. (2007), The physics of the FLUKA code: Recent developments, *Adv. Space Res.*, 40, 1339–1349.
- Cane, H. V. (2000), Coronal mass ejections and Forbush decreases, *Space Sci. Rev.*, 93, 55–77.
- Cucinotta, F. A., J. W. Wilson, and L. W. Townsend (1997), Abrasion–ablation model for neutron production in heavy ion collisions, *Nucl. Phys. A*, 619, 202–212.
- Cucinotta, F. A., M. H. Kim, A. I. Schneider, and D. M. Hassler (2007), Description of light ion production cross sections and fluxes on the Mars surface using the QMSFRG model, *Radiat. Environ. Biophys.*, 46, 101–106.
- Cucinotta, F. A., M. Y. Kim, V. Willingham, and K. A. George (2008), Physical and biological organ dose equivalents for International Space Station astronauts, *Radiat. Res.*, 170, 127–138.
- Cucinotta, F. A., I. Plante, A. L. Ponomarev, and M. Y. Kim (2011), Nuclear interactions in heavy ion transport and event-based risk models, *Radiat. Prot. Dosim.*, 143(2–4), 384–390.
- Cucinotta, F. A., M. Y. Kim, and L. Chappell (2013a), Space radiation cancer risk projections and uncertainties- 2012, NASA TP 2013-217375.
- Cucinotta, F. A., M. Y. Kim, L. Chappell, and J. L. Huff (2013b), How safe is safe enough: Radiation protection for a human mission to Mars, *PLoS One*, 8(10), e74988.
- Gómez-Elvira, J., et al. (2012), REMS: The environmental sensor suite for the Mars Science Laboratory rover, *Space Sci. Rev.*, 170(1–4), 583–640.
- Hassler, D. M., et al. (2012), The Radiation Assessment Detector (RAD) investigation, *Space Sci. Rev.*, 170(1–4), 503–558.
- Hassler, D. M., et al. (2014), The radiation environment on the surface of Mars measured with the Mars Science Laboratory's *Curiosity* rover, *Science*, 343, e1244797.
- Heinbockel, J. H., et al. (2011a), Comparison of the transport codes HZETRN, HETC and FLUKA for a solar particle event, *Adv. Space Res.*, 47, 1079–1088.
- Heinbockel, J. H., et al. (2011b), Comparison of the transport codes HZETRN, HETC and FLUKA for galactic cosmic rays, *Adv. Space Res.*, 47, 1089–1105.
- International Commission on Radiological Protection (2013), Assessment of Radiation Exposures of Astronauts in Space. ICRP Publication 123, 42(4).
- Kim, M. Y., J. W. Wilson, and F. A. Cucinotta (2006), A solar cycle statistical model for the projection of space radiation environment, *Adv. Space Res.*, 37, 1741–1748.
- Kim, M. Y., J. W. Wilson, and F. A. Cucinotta (2012), Description of transport codes for space radiation shielding, *Health Phys.*, 103(5), 621–639.
- McKinney, G. W., D. J. Lawrence, T. H. Prettyman, R. C. Elphic, W. C. Feldman, and J. J. Hagerty (2006), MCNPX benchmark for cosmic ray interactions with the Moon, *J. Geophys. Res.*, 111, E06004, doi:10.1029/2005JE002551.
- Mewaldt, R. A., et al. (2010), Record-setting cosmic-ray intensities in 2009 and 2010, *Astrophys. J. Lett.*, 723(1), doi:10.1088/2041-8205/723/1/L1.
- Nounu, H. N., M. Y. Kim, A. L. Ponomarev, and F. A. Cucinotta (2009), The Use of Pro/ENGINEER CAD Software and Fishbowl Toolkit in Ray-tracing Analysis, NASA/TP-2009-214788, S-1042, NASA Johnson Space Center, Houston, Tex.
- Nymmik, R. A. (2000), Time lag of galactic cosmic ray modulation: Conformity to general regularities and influence on particle energy spectra, *Adv. Space Res.*, 26(11), 1875–1878.
- O'Neill, P. M. (2010), Badhwar-O'Neill 2010 galactic cosmic ray flux model – Revised, *IEEE Trans. Nucl. Sci.*, 57(6), 3148–3153.
- O'Neill, P. M., and C. C. Foster (2013), Badhwar-O'Neill 2011 galactic cosmic ray flux model description, NASA/TP-2-13-217376, 240p.
- Parker, E. N. (1965), The passage of energetic charged particles through interplanetary space, *Planet. Space Sci.*, 13, 9–49.
- Ponomarev, A. L., H. N. Nounu, H. F. Hussein, M. Y. Kim, and F. A. Cucinotta (2007), NASA-developed ProE-based tool for the ray-tracing of spacecraft geometry to determine radiation doses and particle fluxes in habitable areas of spacecraft and in the human body. NASA TP-2007-214770. NASA Johnson Space Center, Houston, Tex.
- Rafkin, S. C. R., et al. (2014), Diurnal variations of energetic particle radiation at the surface of Mars as observed by the Mars Science Laboratory Radiation Assessment Detector, *J. Geophys. Res. Planets*, doi:10.1002/2013JE004525, in press.
- Sato, T., A. Endo, L. Sihver, and K. Niita (2011), Dose estimation for astronauts using dose conversion coefficients calculated with the PHITS code and the ICRP/ICRU adult reference computational phantoms, *Radiat. Environ. Biophys.*, 50, 115–123.
- Slaba, T. C., S. R. Blattnig, S. K. Aghara, L. W. Townsend, T. Handler, T. A. Gabriel, L. S. Pinsky, and B. Reddell (2010), Coupled neutron transport for HZETRN, *Radiat. Meas.*, 45, 173–182.

- Slaba, T. C., S. R. Blattnig, B. Reddell, A. Bahadori, R. B. Norman, and F. F. Badavi (2013), Pion and electromagnetic contribution to dose: Comparisons of HZETRN to Monte Carlo results and ISS data, *Adv. Space Res.*, *52*, 62–78.
- Tylka, A. J., J. H. Adams Jr., P. R. Boberg, B. Brownstein, W. F. Dietrich, E. O. Flueckiger, E. L. Petersen, M. A. Shea, D. F. Smart, and E. C. Smith (1997), CREME96: A revision of the cosmic ray effects on micro-electronics code, *IEEE Trans. Nucl. Sci.*, *44*(6), 2150–2160.
- Wilson, J. W., L. W. Townsend, J. L. Shinn, F. A. Cucinotta, R. C. Costen, F. F. Badavi, and S. L. Lamkin (1994), Galactic cosmic ray transport methods: Past, present, and future, *Adv. Space Res.*, *14*, 841–852, doi:10.1016/0273-1177(94)90549-5.
- Wilson, J. W., R. K. Tripathi, G. D. Qualls, F. A. Cucinotta, R. E. Prael, J. W. Norbury, J. H. Heinbockel, and J. Tweed (2004), Space radiation transport model development, *Adv. Space Res.*, *34*, 1319–1327.
- Zeitlin, C. J., et al. (2013), Measurements of energetic particle radiation in transit to Mars on the Mars Science Laboratory, *Science*, *340*, 1080–1084.